

## The structure and elastic properties of phosphorene edges

This content has been downloaded from IOPscience. Please scroll down to see the full text.

2015 Nanotechnology 26 235707

(<http://iopscience.iop.org/0957-4484/26/23/235707>)

View [the table of contents for this issue](#), or go to the [journal homepage](#) for more

Download details:

IP Address: 210.13.109.81

This content was downloaded on 07/09/2015 at 08:32

Please note that [terms and conditions apply](#).

# The structure and elastic properties of phosphorene edges

V Sorkin and Y W Zhang

Institute of High Performance Computing, A\*Star, 138632, Singapore

E-mail: [sorkinv@ihpc.a-star.edu.sg](mailto:sorkinv@ihpc.a-star.edu.sg) and [zhangyw@ihpc.a-star.edu.sg](mailto:zhangyw@ihpc.a-star.edu.sg)

Received 2 February 2015, revised 30 March 2015

Accepted for publication 13 April 2015

Published 21 May 2015



## Abstract

We investigated the edge atomic structures and elastic properties of defect-free phosphorene nanoribbons (PNRs). Density functional tight binding simulations were used to optimize two main edge configurations: armchair (AC) and zigzag (ZZ). It was found that the energy relaxation of PNRs leads to the noticeable changes in edge atomic configurations. The effective width of the edge region, which includes all the atoms involved in the edge relaxation, was found to contain approximately three atomic rows near the edge for both AC and ZZ PNRs. We further extracted the edge stress and modulus for the ZZ and AC edges. Both the AC and ZZ edge stresses of PNRs are positive, indicating tensile stress at the edges. In addition, both the AC and ZZ edge moduli are positive. However, the edge elastic modulus and edge stress of ZZ PNRs are about three times larger than those of AC PNRs. Furthermore, we showed that the tensile edge stresses along ZZ and AC edges are able to cause distortion in freestanding phosphorene nanoribbons. Our results highlight the importance of accounting for edge stresses in the design and fabrication of PNRs.

Keywords: phosphorene nanoribbons, edge structure, edge relaxation, edge stress, residual edge strain, edge moduli, warping

(Some figures may appear in colour only in the online journal)

## 1. Introduction

Phosphorene, a single layer of black phosphorus, has attracted considerable attention recently due to its direct band-gap semiconducting characteristics. Initially, few-layer phosphorene was obtained through mechanical exfoliation [1–4]. Very recently, monolayer phosphorene was also obtained by mechanical cleavage, followed by a subsequent plasma thinning process [5]. Phosphorene is being considered as a promising electronic material in addition to graphene [6, 7], boron nitride [8–10], and transition metal dichalcogenides [11–14]. Although its two-dimensional lattice structure is similar to graphene, it is a direct band-gap semiconductor with a sizable fundamental band gap, ideal for making field-effect transistors [4, 15–18], especially for flexible electronics [19–21]. In addition, other interesting applications have also been demonstrated, such as gas sensors [22], thermo-electrics [23–25], Li-ion batteries [26, 27], p–n junctions [28–31], photo catalysts [32] and solar-cell systems [29, 33, 34].

Besides its direct band gap characteristics, phosphorene also exhibits a relatively high carrier mobility with a magnitude of  $\sim 300\text{--}1000\text{ cm}^2\text{ V}^{-1}\text{ s}^{-1}$  [17, 21, 35, 36], which is three to five times higher than  $\text{MoS}_2$  [13, 35]. Its puckered structure also gives rise to direction-dependent carrier mobility. Using density functional theory calculations, Peng *et al* [37] demonstrated that the effective masses of charge carriers in the armchair (AC) direction are an order of magnitude smaller than those in the zigzag (ZZ) direction, indicating that the AC direction is much favored for carrier transport. Also, this large anisotropy implies that electrons and holes can be considered as classical particles along the ZZ direction, but as relativistic particles along the AC direction. This unexpected combination of classical and relativistic properties in phosphorene creates a unique opportunity for revealing new fundamental physical principles and also for novel applications. In addition, the effective masses can be substantially modified by strain [37, 38]. It was shown that under in-plane (transverse) compressive strain, phosphorene is able to transform into an indirect gap semiconductor, while under out-of-plane

(perpendicular) compression, it transforms into a metal [35, 39]. The rich varieties of electronic properties under strain [40–43] and electric field [4, 19, 44] make phosphorene promising for effective strain engineering [40].

Similar to the electronic properties, the mechanical properties of phosphorene were also found to be highly anisotropic due to its puckered structure [40–45, 46]. First-principles calculations [40, 45, 47] showed that phosphorene can be stretched up to  $\sim 40\%$  before breaking along the AC direction. This large tensile strain was attributed largely to the flattening of the puckers, rather than to the stretching of P–P bonds [40]. Compared to graphene, phosphorene possesses a smaller in-plane Poisson's ratio along both the AC and ZZ directions [42], and a negative out-of-plane Poisson's ratio for uniaxial deformation along the ZZ direction [42, 46, 47].

Similar to the charge transport, the thermal transport of phosphorene is also highly anisotropic [24, 25, 48]. The thermal conductivity along the ZZ direction was found to be about twice that along the AC direction [48]. Remarkably, this anisotropy can be tuned by applied strain [24], which is beneficial for thermal management in phosphorene-based electronics and optoelectronic devices. Although the thermal conductivity of phosphorene is relatively low  $\sim 30 \text{ W m}^{-1} \text{ K}^{-1}$  [48] (the thermal conductivity for silicon is  $150 \text{ W m}^{-1} \text{ K}^{-1}$  [49, 50] or that for graphene is  $\sim 2000\text{--}5000 \text{ W m}^{-1} \text{ K}^{-1}$  [51]), it possesses a high value of the figure of merit (ZT), and thus is being considered as a promising thermo-electric material [23, 25, 52].

Since only finite-size phosphorene is used in practical applications, its edge structures and properties must be taken into consideration. In fact, it was found that the edges of phosphorene can introduce fundamental changes in electronic properties. For example, phosphorene nanoribbons (PNRs) are indirect band gap semiconductors, while phosphorene monolayer is direct band gap semiconductor [33, 53–57]. Besides, first-principle calculations [25, 54, 55] showed that the band gap of AC PNRs decreases monotonically with increasing the nanoribbon width. In contrast to the AC edges, the properties of PNRs with ZZ edges are controversial. On the one hand, it was claimed that the ZZ edges introduce metallic edge states and thus the ZZ PNRs are metals [53]. On the other hand, it was claimed that the ZZ PNRs are semiconductors, and their band gaps can be insensitive to [54] or even decrease, following a power law, with the nanoribbon width [18, 44, 54, 57–59]. Nevertheless, it was found that band gaps of both AC and ZZ PNRs can be efficiently tuned by in-plane (transverse) electric field, although they are not sensitive to out-of-plane (perpendicular) fields [18].

Although extensive research has been carried out to explore the electronic properties of PNRs, their mechanical properties, especially those related to their edges are largely unexplored. It is noted that the structure and mechanical properties of graphene nanoribbons (GNRs) and nanotubes were widely studied [60–69]. It is now known that graphene has four experimentally confirmed periodic edge terminations, ZZ, AC as well as reconstructed ZZ(57), and extended Klein edge [70]. Koskinen *et al* [71] found that ZZ edges of graphene spontaneously reconstruct to acquire ZZ(57) edge

structure with the lowest energy among the all possible edge geometries. The reconstruction changes electronic structure and self-passivates the graphene edges [71]. Recently the fourth periodic edge of graphene called the extended Klein edge, predicted by Klein [72], has been experimentally confirmed [73].

In addition to the atom positions near the edges, the edge termination changes the charge distribution in GNRs and carbon nanotubes (CNTs) [74–76]. The edge effect in CNTs results in the voltage generation, since the charges at the ends of the nanotube are much larger than those in the middle [74]. The charges rapidly decrease in magnitude from the edges of the nanotube. Density functional theory (DFT) calculations indicated that nanotubes with different chiralities have significantly different charges at the ends of nanotubes [75]. The magnitude of the charges at the ends of the ZZ single wall carbon nanotube (SWCNT) is  $\sim 5$  times greater than that of the AC SWCNT. Similarly, the edge effect in GNRs leads to the highly non-uniform charge distribution in the in-plane direction normal to the GNR edges [70, 77].

Another important feature of graphene edges is their intrinsic stress. It was found that graphene edges can be under compression or tension, depending on the edge structures [60–66, 68]. The general understanding is that since the under-coordinated edge atoms have fewer neighbors than the bulk atoms, their bonding configurations are different from the bulk. If the atomic bonds at the edges are shorter than those in the bulk, the edge will be under tension; otherwise, the edge will be under compression. Especially for narrow GNRs (width  $< 20 \text{ \AA}$ ), the intrinsic stress is sufficiently large to overcome the out-of-plane stiffness, leading to a mechanical instability, which results in a twisted conformation of GNRs [60, 63, 69]. It was also shown that as the width increases, a compressive edge stress can lead to warping of GNRs, while a tensile edge stress can lead to curling and rippling of GNRs [60, 62, 63, 65]. In even wider GNRs, the stress is released by forming frill wavy patterns along the graphene edges [69].

Our goal is to study the edge structures and mechanical properties of PNRs. More specifically, we examine the structure and stability of phosphorene edges, and then extract their mechanical properties, such as edge stress and edge modulus. In addition, we would also like to answer the following question: Is the edge stress sufficiently large to cause warping or rippling instability of PNRs? To answer these questions, we perform density functional tight binding (DFTB) calculations, focusing on two primary edges of phosphorene: AC and ZZ.

## 2. Computational model

We use tight-binding (TB) method [78–80] to study edge structures and properties of the PNRs. The TB method occupies an important place in the hierarchy of techniques available for the atomistic modeling of phosphorene. The DFT method applied to investigate nanoscale phosphorene-based systems is very accurate, but computationally intense and expensive. The simulations for medium or large scale

**Table 1.** Geometry of phosphorene unit cell obtained with the DFT and DFTB methods. The DFT data are taken from [29]. Refer to figure 1(a) for the atom, bond and angle notations.

Unit cell	DFT	DFTB	Error (%)
AB	2.24 Å	2.49 Å	11.2
AC	2.28 Å	2.39 Å	4.8
<ABD	96.13°	95.67°	0.5
<BAC	103.36°	96.17°	6.7

systems are not feasible by this method. Molecular dynamics simulations cannot be used either, since reliable interatomic potential for phosphorene is absent. In this context, empirical TB method can be employed to address the size problems.

In our simulations of PNRs, we apply DFTB method, which merges the reliability of DFT with the simplicity and efficiency of TB [81–83]. It is based on a second-order expansion of the Kohn–Sham total energy in DFT [84–86] with respect to charge density fluctuations. The zeroth order approach is equivalent to a standard TB scheme. At the second order, one obtains a transparent, parameter-free, and readily calculable expression for generalized Hamiltonian matrix elements [81–83]. Besides the usual band structure and short-range repulsive terms, the final approximate Kohn–Sham energy includes Coulomb interactions between charge fluctuations, which accounts for long-range electrostatic forces between point charges. In addition, this method handles long-range dispersive interactions by empirical corrections.

In DFTB, the new self-consistent-charge scheme is applied to alleviate the deficiencies within the standard TB approach, which lacks reliability and transferability due to the parameterization with respect to a finite set of equilibrium structures. The DFTB method offers much higher degree of transferability and universality for both ground-state and excited-state properties. It provides accurate results at a fraction of the computational cost of DFT calculations [81–83]. Structural, mechanical and electronic properties of phosphorene nanotubes were studied previously by DFTB [87]. In addition, the electronic properties of phosphorene layers (from one to four) were also studied by TB [44, 53, 88, 89].

First, we applied the DFTB method to optimize the geometry of phosphorene unit cell obtained by DFT calculations [29, 56]. Periodic boundary conditions were applied in all directions. A vacuum slab with the width of 16 Å was added in the direction perpendicular to the phosphorene sheet to avoid self-interaction due to periodic boundary conditions. The k-point set for the Brillouin-zone integration was selected by using the Monkhorst–Pack method [90–92]. To simulate the phosphorene sheet, we used a  $4 \times 4 \times 2$  Monkhorst–Pack sampling set (the numbers denote divisions along three reciprocal space axes  $k_x$ ,  $k_y$  and  $k_z$ , respectively). Following the DFTB calculations for phosphorene nanotubes [87], we specified the s-, p- and d-orbitals for each phosphorene atom. The Slater–Koster files [78, 93] for phosphor atoms were taken from ‘MATSCI’ set [94, 95].

Upon geometry optimization, the phosphorene unit cell was slightly modified (see table 1 and figure 1), which is expected since the DFTB method is more computationally effective but less accurate than DFT. The largest deviation from DFT results for the unit cell geometry was ~11% (see table 1).

Using the DFTB optimized unit cell, we constructed a phosphorene monolayer. PNRs with AC and ZZ edges were cut from the monolayer as shown in figure 1. In our simulations, periodic boundary conditions were applied in all three directions. The free edges of PNRs were oriented in parallel to the direction of the uniaxial strain (along the X-axis). To avoid self-interaction of the PNRs due to periodic boundary conditions, the vacuum slabs were added along the free edges, and also in the direction perpendicular to the PNRs. The width of each vacuum slab was 16 Å. The Monkhorst–Pack grid [90, 91] with an  $8 \times 4 \times 1$  sampling set was used for the Brillouin-zone integration, and the s-, p- and d-orbitals for each phosphor atom were specified.

Uniform uniaxial tensile (or compressive) strain was applied quasi-statically at zero temperature. At each step, a PNR was uniformly strained along the X-axis. The uniaxial strain was incrementally added with a strain step of 0.005. Consequently, the geometry of the PNRs was optimized by using conjugate gradient technique, which minimizes the total energy of the system. Self-consistent charge calculations were performed at each step of energy minimization.

The simulations were carried out for the AC and ZZ nanoribbons of various widths. The width of the nanoribbons was varied from ~10 to ~30 Å. The number of atoms was in the range between ~100 and ~300 atoms. This number of atoms is larger than the number phosphorous atoms used in current DFT simulations of PNRs [25, 54, 57], where it was limited by ~100 atoms. By using the DFTB simulations, we were capable not only to investigate larger samples, but to examine their deviations from the reference state manifesting itself in edge relaxation and edge warping of PNRs. The length of nanoribbons was  $L = 45.7$  Å and  $L = 44.3$  Å, for the AC and ZZ nanoribbons, respectively. The number of atomic rows (parallel to the X-axis) for AC PNR was varied from  $n = 6$ –16 (see figure 1(d)), and for ZZ PNR from  $n = 10$ –30 (see figure 1(e)).

### 3. Results and discussion

#### 3.1. Edge structures

To study the structures and properties of PNR edges, we constructed PNRs and optimized their geometries by minimizing the potential energy. In that follows, we present the results of geometry optimization for an AC PNR with  $n = 10$  rows or  $w = 16.7$  Å and a ZZ PNR with  $n = 18$  rows or  $w = 17.2$  Å, respectively. The initial and final geometries of the two PNRs are shown in figures 2 and 3, respectively (the edge atoms are highlighted).

For the AC edge geometry as shown in figure 2, each atom located at the edge of the AC PNR has one dangling



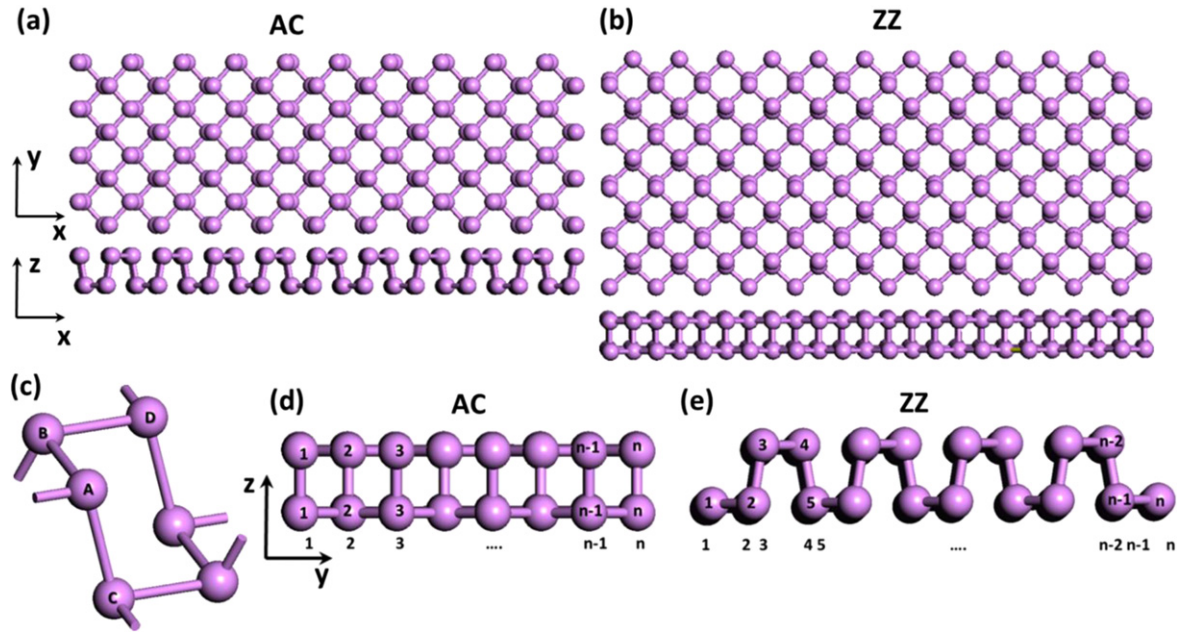


**Figure 1.** (a) Phosphorene nanoribbon with armchair edges: top and side view; (b) phosphorene nanoribbon with zigzag edges: top and side view; (c) unit cell of phosphorene; numeration of the atomic rows from 1 to  $n$  in the AC (d) and ZZ (e) phosphorene nanoribbons (front view). The top and bottom rows in the AC PNR are identical, but different in the ZZ PNRs.

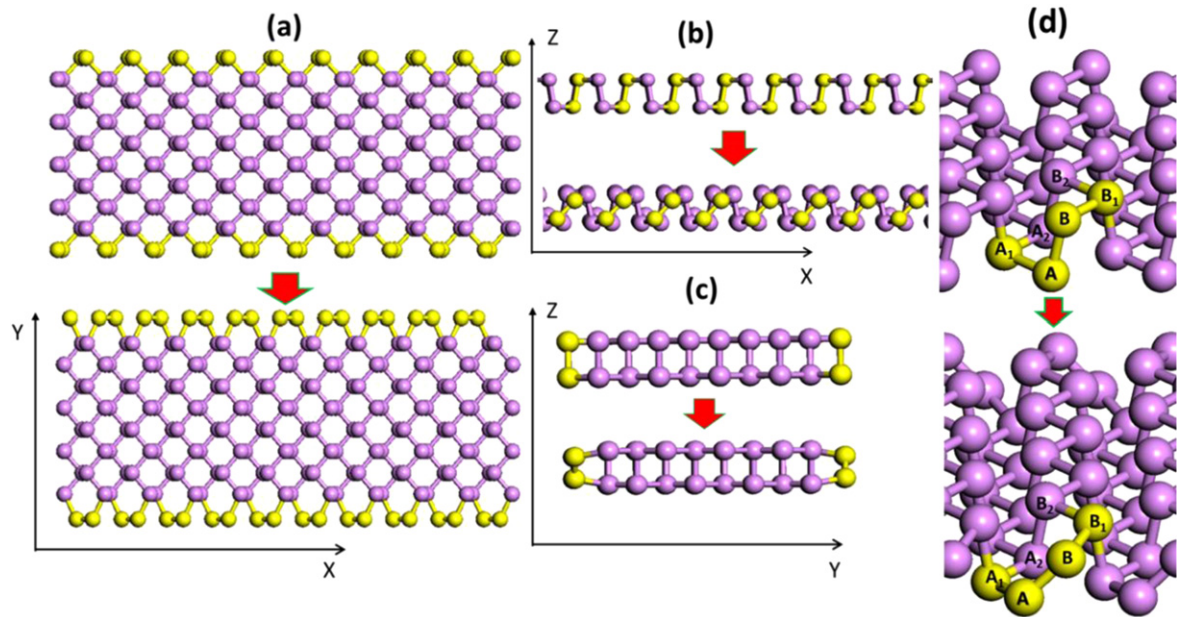


**Figure 2.** Initial and final configurations of the AC PNR with  $n = 10$  rows or  $w = 16.7$  Å upon energy relaxation: (a) top view, (b) side view, (c) front view (cross-section), and (d) zoom-in view of a segment of the PNR: atom A with a dangling bond, and its nearest ( $A_1$  and  $B_1$ ) and next nearest neighbors ( $A_2$  and  $B_2$ ). The edge atoms are highlighted in yellow.

bond. Upon energy relaxation, the bond contraction and reorientation at the edges are evident. To investigate edge relaxation in details, we selected two nearest edge atoms (atoms A and B in figure 2(d)), each with one dangling bond. Their nearest neighbors are: the  $A_1$ - and B-atoms for the A-atom, and the A-atom and  $B_1$ -atoms for the B-atom. The bond length between these atoms before and after the energy relaxation is listed in table 2. In addition, we also measured the angles formed by these atoms: the angles between the

vertically and horizontally oriented bonds ( $\angle A_1AB$  and  $\angle ABB_1$ ), and the angles between the horizontally oriented bonds: ( $\angle AAA_2$  and  $\angle BB_1B_2$ ). As can be seen in table 2, the largest bond length contraction is between the two edge atoms (AB) with dangling bonds. The bond length between the A and B atoms decreases by  $\sim 12\%$ ; and the bond rotates by  $36^\circ$  in the XZ plane. In the presence of dangling bonds, these atoms move closer to compensate for electronic density deficiency. The changes in the length of the neighboring

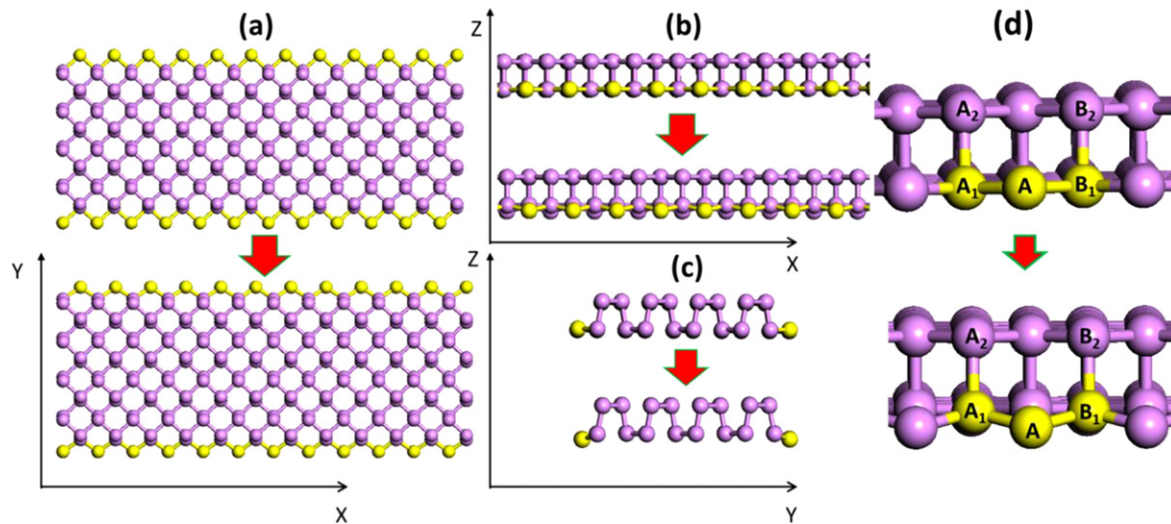


**Figure 3.** The initial and final configurations of the ZZ PNR with  $n=18$  rows or  $w=17.2$  Å upon energy relaxation: (a) top view, (b) side view, (c) front view (cross-section), and (d) zoom-in view of a segment of the PNR, atom (A) with a dangling bond, and its nearest ( $A_1$  and  $B_1$ ) and next nearest neighbors ( $A_2$  and  $B_2$ ). The edge atoms are highlighted in yellow.

bonds ( $AA_1$ ,  $BB_1$ ,  $A_1A_2$  and  $B_1B_2$ ) are minor (see table 2). In contrast to the bond length, the changes in the angles between these atoms are even more significant ( $\sim$ up to 20%).

For the ZZ PNR, the changes in the nanoribbon geometry due to energy relaxation are most noticeable in the side view and front (cross-section) views in figures 3(b) and (c). It is seen that the highlighted edge atoms are displaced along the Z-axis by  $\sim 0.5$  Å. We examined the edge relaxation by focusing on an edge atom with a dangling bond (the A-atom in figure 3(d)) and its two nearest ( $A_1$ ,  $B_1$ ) and next nearest ( $A_2$ ,  $B_2$ ) neighbors. The obtained lengths of the  $AA_1$  and  $AB_1$  bonds, and their neighboring  $A_1A_2$  and  $B_1B_2$  bonds before and after energy relaxation are given in table 3, together with the measured in-plane  $\angle A_1AB_1$  and out-of-plane angles  $\angle AA_1A_2$  and  $\angle AB_1B_2$  before and after edge relaxation. The most significant change is in the length of the  $AA_1$  and  $AA_2$  bonds (formed by the edge A-atom with a dangling bond). The contraction of these bonds is about  $\sim 10\%$ . In addition, the change in the in-plane and out-of-plane angles is also large  $\sim 14\%$ .

Compared to the AC PNR upon energy relaxation, the change in the geometry configuration of the ZZ PNR is moderate (see figures 2 and 3). In general, a PNR can be partitioned into two planes, that is, the upper and lower planes (see figures 2(b) and 3(b)), due to its puckered structure. In the case of the AC PNR, the edge atoms with dangling bonds belong to both planes, while all edge atoms of the ZZ PNR reside only in the lower plane. The number of edge atoms with dangling bond per unit length for the ZZ PNR is  $\rho=0.27$  Å $^{-1}$ , which is only half of that for the AC PNR ( $\rho=0.44$  Å $^{-1}$ ). Therefore, the effect of energy relaxation is less pronounced for the ZZ PNR.

To characterize the extent of the observed edge relaxation, we considered different rows of the nanoribbon atoms oriented along the X-axis. An index (row number) was assigned to each row (see the row numeration in figures 1(d)

and (e)). We measured the length of the vertically-oriented bonds in each row (see figure 4(a)) and the horizontally-oriented bonds between the adjacent rows (see figure 4(b)). As can be seen from figure 4(a), the substantial change in the length of the vertically-oriented bonds is observed in the first edge row of the AC PNR, while the bond relaxation in the ZZ PNR is insignificant. However, the edge relaxation of the ZZ PNR results in a marked change in the length of the horizontally-oriented bonds (see figure 4(b)) for two edge rows of atoms. The deviation from the bulk value, indicated by the dashed line, is rather small for the remaining inner rows.

Next, we calculated the potential energy of per atom in each nanoribbon row. Since periodic boundary conditions are applied along the X-direction, the potential energy per atom is the same for all atoms within an atomic row oriented along the X-axis. Therefore, it is convenient to present the potential energy per atom as a function of the atomic row number (see figure 5). Note that the AC PNR has mirror symmetry relative to the XY plane passing through the center of its cross-section (see figure 1(e)). The ZZ PNR does not have this mirror symmetry (see figure 1(d)). Thus in the case of the AC PNR, two rows of atoms, which have the identical X- and Y-coordinates but different Z-coordinates (upper and lower rows) are considered as one row since the atoms in these two rows have the identical potential energy. For the ZZ PNR, we consider each atomic row separately.

The variation of the potential energy per atom with the atomic row is shown in figure 5, in which the colored nanoribbon cross-sections are used to visualize the potential energy distribution across the sample. The edge atoms of the first and last rows (red atoms in figure 5) have the highest energy. Their potential energy is by  $\sim 10\%$  higher than the energy of the middle row atoms (blue atoms in figure 5) in the AC PNR, while for the ZZ PNR, the difference is  $\sim 18\%$ . The potential energy per atom in the 2nd edge row (gray atoms in figure 5) of the AC PNR is lower than in the 1st one, while the

**Table 2.** Bond lengths and angles at the AC edge of the PNR with  $n = 10$  rows or  $w = 16.7$  Å before and after energy relaxation. See figure 2(d) for the notation of bonds and angles.

Bond	Bond length before energy relaxation	Bond length after energy relaxation	Change
AB	2.392 Å	2.091 Å	−12.6%
AA <sub>1</sub> , BB <sub>1</sub>	2.488 Å	2.465 Å	−1%
A <sub>1</sub> A <sub>2</sub> , B <sub>1</sub> B <sub>2</sub>	2.488 Å	2.423 Å	−2.7%
Angle	An angle before energy relaxation	Angle after energy relaxation	Change
<A <sub>1</sub> AB, <ABB <sub>1</sub>	96.32°	116.12°	+20.6%
<AA <sub>1</sub> A <sub>2</sub> , <BB <sub>1</sub> B <sub>2</sub>	94.75°	110.51°	+16.6%

potential energy of the 3rd row is lower than the 2nd one. In contrast, the potential energy per atom in the 3rd row of the ZZ PNR is higher than the potential energy in the 2nd one.

Examination on these two cases demonstrates that approximately three atomic rows near the edges are substantially changed during geometry optimization. It can be postulated that these three edge rows primarily constitute the edge region, and the rest can be considered as the interior (bulk) region. In order to test the validity of this postulation, we varied the width of PNRs from  $\sim 10$  to  $\sim 30$  Å, and then optimized their geometries. The obtained bond lengths and potential energy distributions for the AC and ZZ PNRs of various widths are shown in figure 6 and figure 7, respectively. As can be seen from these figures, the substantial changes in both the bond length and potential energy are observed in the three atomic rows near the edges. It should be noted that ultra-narrow PNRs must be excluded from this analysis since they cannot be properly divided into the edge and interior regions. We found that the width of AC PNRs must exceed  $w \sim 13$  Å, that is, 8 atomic rows (see figures 6(a) and 7(a)), while the width of ZZ PNRs must exceed  $w \sim 9$  Å, that is, 10 atomic rows (see figures 6(b) and 7(b)), in order to partition the PNRs into the edge and bulk regions. With this partition, we can clearly distinguish the bulk and edge regions, and proceed to study the edge properties.

### 3.2. Edge elastic properties

In addition to the structural changes, the edge relaxation can also lead to edge stress. In order to investigate the edge stress and other edge properties, we applied the method developed in [60, 62, 65]. Following this method, we subjected PNRs to a uniform uniaxial strain,  $\varepsilon$ , along the  $X$ -axis. The potential energy per unit length of the PNR is given as a quadratic function of strain [62]:

$$U(\varepsilon, w) = U_0 + 2\tau\varepsilon + E_e\varepsilon^2 + \frac{1}{2}E_b\varepsilon^2w, \quad (1)$$

where  $U_0$  is the potential energy at zero strain,  $E_b$  and  $E_e$  denote the bulk and edge elastic modulus, respectively,  $\tau$  is the edge stress, and  $w$  is the nanoribbon width. The second and third terms in the right side of this equation describe the edge effects. An effective elastic modulus,  $E_{\text{eff}}$ , for the PNR

can be defined as [62]:

$$E_{\text{eff}}(w) = \frac{\partial^2 U}{\partial \varepsilon^2} \Big|_{\varepsilon=0} = E_b + \frac{2E_e}{w}. \quad (2)$$

It is calculated as a second derivative of the PNR potential energy per unit length at zero strain  $\varepsilon = 0$ .

By applying uniaxial strain, we calculated the potential energy as a function of applied strain (see figures 8(a) and (b)) which shows the potential energy per atom for the AC and ZZ PNRs of various widths). It is seen that the potential energy reaches its global minimum at a non-zero strain, called the residual strain,  $\varepsilon_r$ , which is plotted in figure 8(d) for both the AC (red circles) and ZZ (blue squares) PNRs.

The relation between the residual strain, edge stress and effective elastic modulus is given by [62]:

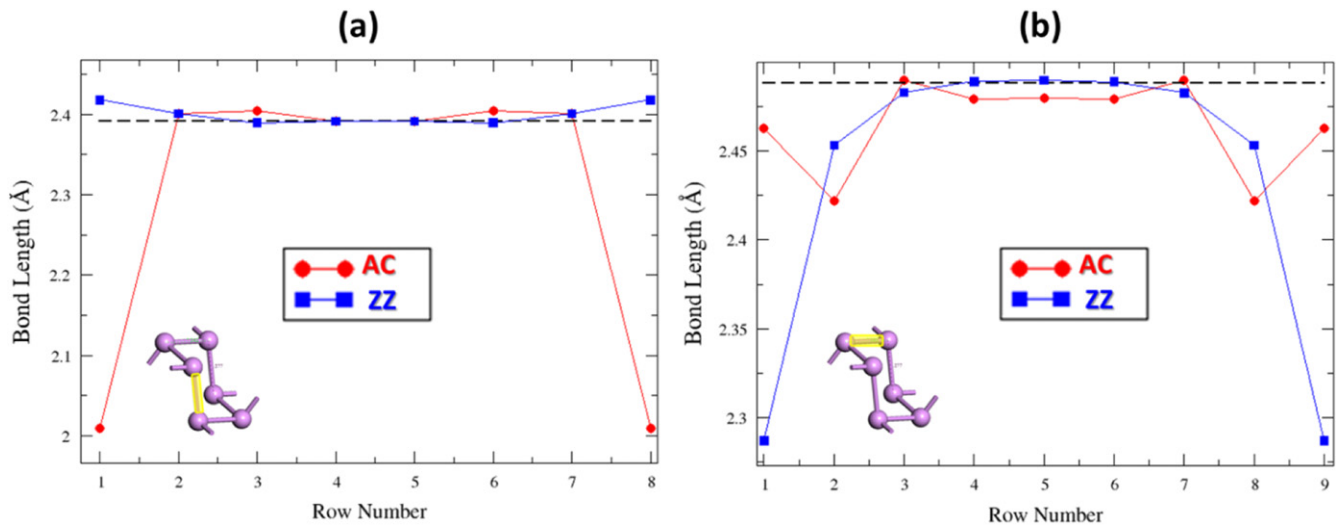
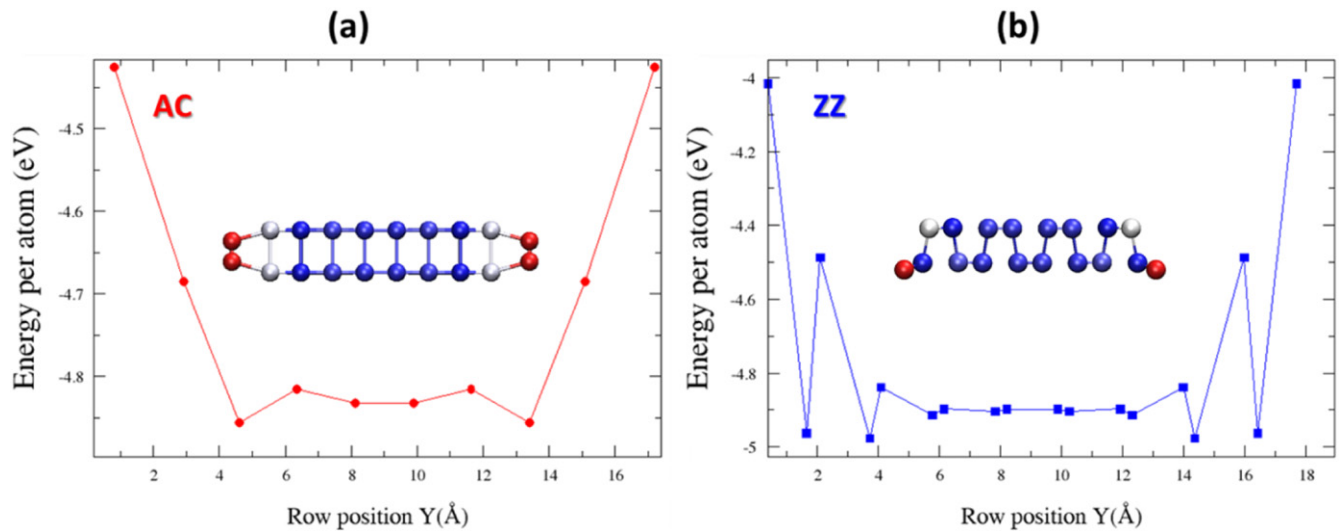
$$\varepsilon_r(w) = \frac{-2\tau}{w\left(E_b + \frac{2E_e}{w}\right)} = \frac{-2\tau}{wE_{\text{eff}}}. \quad (3)$$

The effective elastic modulus is calculated by using the potential energy in figures 8(a) and (b) as:  $E_{\text{eff}} = \frac{1}{w} \frac{\partial^2 U}{\partial \varepsilon^2}$  and plotted in figure 8(c). The effective elastic modulus of PNRs with ZZ edges is notably larger than PNRs with AC edges. Moreover, the effective moduli for both types of edges are larger than the corresponding bulk moduli, and the difference is especially significant when PNRs are narrow. As the width of nanoribbons increases, the edge effects gradually diminish, and the value of the effective elastic modulus,  $E_{\text{eff}}$ , approaches to the corresponding bulk value. By fitting the effective elastic modulus to the PNR width, the bulk elastic and edge elastic modulus can be extracted [60, 62]. The residual strain can be obtained by finding the strain corresponding to the global minimum of the potential energy and plotted in figure 8(d). The edge stress can be obtained from equation (3) with knowledge of the residual strain, effective elastic modulus, and width of PNRs. The calculated values of the bulk and edge elastic modulus, as well as the edge stress are given in table 4. It is seen that there are large differences in the mechanical properties of the two edges: The edge elastic constant, edge stress and Young's modulus of the ZZ PNRs are at least three times larger than those of AC PNRs, indicating large mechanical anisotropy in PNRs. Interestingly, the edge stresses for both ZZ and AC edges are positive, indicating that these edges are under tension. It is noted that these ribbon edges are similar to that of the reconstructed GNRs, which also exhibit positive edge stresses [62, 65].



**Table 3.** Bond lengths and angles at the edge of ZZ PNR with  $n = 18$  rows or  $w = 17.2$  Å before and after energy relaxation. See figure 3(d) for the notation of bonds and angles.

Bond	Bond length before energy relaxation	Bond length after energy relaxation	Change
$A_1A$ , $AB_1$	2.488 Å	2.243 Å	−9.8%
$A_1A_2$ , $B_1B_2$	2.392 Å	2.462 Å	+2.9%
Angle	An angle before energy relaxation	Angle after energy relaxation	Change
$\angle A_1AB_1$	94.75°	104.92°	+10.7%
$\angle AA_1A_2$ , $\angle AB_1B_2$	96.32°	109.6°	+13.8%

**Figure 4.** Length of the vertically-oriented (a) and horizontally-oriented (b) bonds versus the row number for the AC (red circles) and ZZ (blue squares) PNRs. Bond orientation is highlighted in the plot inset. The first and the last rows correspond to the left and the right edges of the PNRs. The dashed line indicates bond length for bulk phosphorene (obtained by using periodic boundary conditions applied in both the  $X$  and  $Y$  directions, with the added vacuum region along the  $Z$  direction only).**Figure 5.** Potential energy distribution across the AC (a) and ZZ (b) PNRs. The high-energy edge atoms are marked in red and the low-energy interior atoms in blue. The width of the AC PNR is  $n = 10$  rows or  $w = 16.37$  Å and of the ZZ PNR is  $n = 18$  rows or  $w = 17.32$  Å.

First, we compare edge energies of GNRs and PNRs. Graphene edges have an extra edge energy  $\gamma$ , and its values calculated by DFT is  $\gamma_{ZZ} = 1.53 \text{ eV Å}^{-1}$  (or 3.77 eV per atom) for the ZZ edge, and  $\gamma_{AC} = 1.24 \text{ eV Å}^{-1}$  (or 2.65 eV per atom) for the AC edge [63]. In phosphorene, the values calculated

by DFTB are  $\gamma_{ZZ} = 1.4 \text{ eV Å}^{-1}$  (or 0.38 eV per atom) for the ZZ edge, and  $\gamma_{AC} = 0.11 \text{ eV Å}^{-1}$  (or 0.23 eV per atom) for the AC edge. The edge energy per atom was obtained as:  $\Delta E = \frac{1}{3}(E_1 + E_2 + E_3) - E_b$ , where  $E_i$  is the energy of an atom in the  $i$ th edge row ( $i = 1, 2, 3$ ) and  $E_b$  is the energy of a



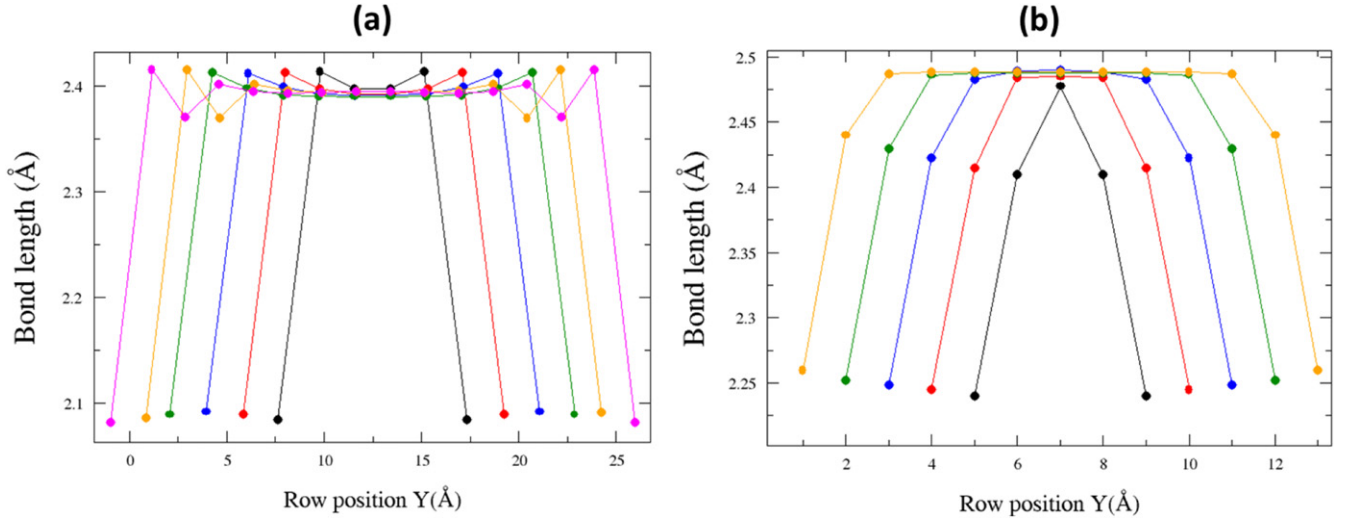


**Figure 6.** Length distribution of (a) vertically-oriented bonds across AC PNRs and (b) horizontally-oriented bonds across ZZ PNRs. Bond length is calculated for each nanoribbon row. The width of AC PNRs varies from 9.34 to 26.29 Å (black circles  $w=9.34$  Å, red circles  $w=9.34$  Å, blue circles  $w=16.37$  Å, green circles  $w=19.9$  Å, yellow circles  $w=23.4$  Å and magenta circles  $w=26.29$  Å). The width of ZZ PNRs is varied from 9.09 to 26.3 Å (black circles  $w=9.09$  Å, red circles  $w=13.22$  Å, blue circles  $w=17.32$  Å, green circles  $w=22.06$  Å and yellow circles  $w=26.3$  Å). It is seen that the changes in the bond length mainly occur in the first a few rows near the edges.

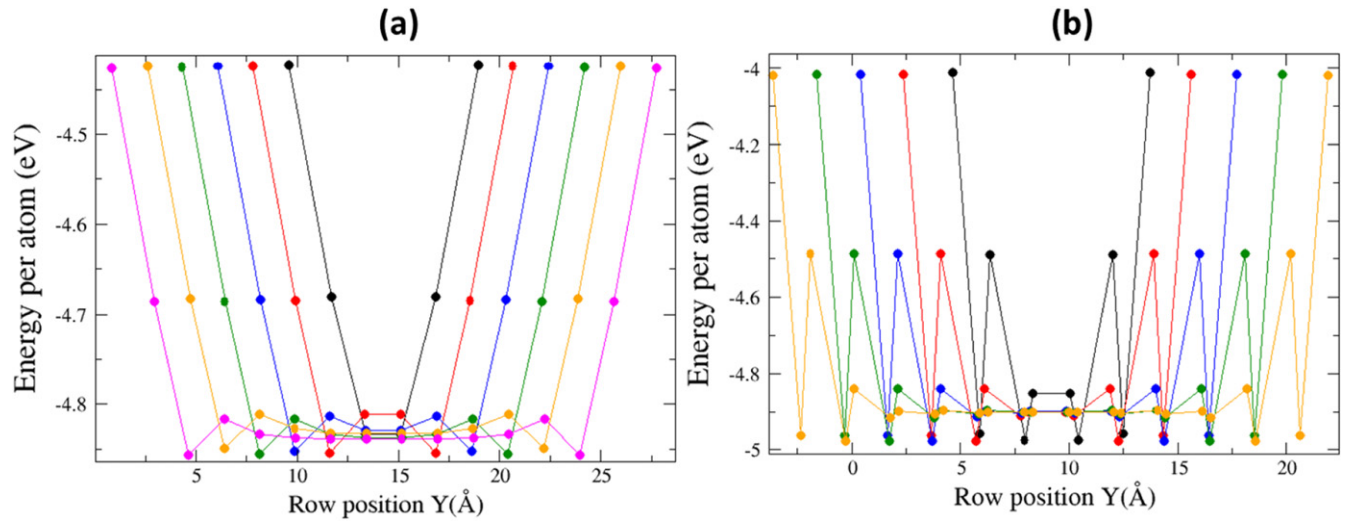


**Figure 7.** Potential energy distribution across the AC (a) and ZZ (b) PNR samples. Width of the nanoribbons is varied from 9 to 27 Å. The width of AC PNRs varies from 9.34 to 26.29 Å (black circles  $w=9.34$  Å, red circles  $w=9.34$  Å, blue circles  $w=16.37$  Å, green circles  $w=19.9$  Å, yellow circles  $w=23.4$  Å and magenta circles  $w=26.29$  Å). The width of ZZ PNRs is varied from 9.09 to 26.3 Å (black circles  $w=9.09$  Å, red circles  $w=13.22$  Å, blue circles  $w=17.32$  Å, green circles  $w=22.06$  Å and yellow circles  $w=26.3$  Å). The energy of the atoms in the rows near the edges is larger than the energy in the interior. The substantial changes in the potential energy are in the first three atomic rows near the edges.

bulk atom. The edge energy is given by  $\gamma = \Delta E_{\text{r}}/L$ , where  $N_{\text{r}}$  is the number of atoms in a row and  $L$  is the nanoribbon length. The edge energies in PNRs are lower than those in GNRs. However, similar to graphene, the AC edge energy  $\gamma_{\text{AC}}$  is lower than the ZZ edge energy  $\gamma_{\text{ZZ}}$ , since each ZZ edge atom contains unreconstructed dangling bond, while in the AC case, the adjacency of the edge atoms permits dangling bond reconstruction, which reduces edge energy.

Next, we note that the difference between the graphene and PNRs is in the sign of the edge stress. The nanoribbon edge can be represented as an elastic string that is either

stretched or compressed, and glued to the internal region (bulk). In GNR, the edge is represented by a compressed string, which exerts the tensile forces on the GNR. The edge stress is tensile, since bonds formed by the edge atoms are elongated, compared to the bulk [60, 63]. In contrast, the bonds formed by the edge atoms in phosphorene are shortened in comparison to the bonds in the bulk, and the compressive forces are exerted by the edge atoms on the PNR. Therefore the residual strain in graphene is tensile, while in PNRs compressive.

Finally, we compare the bulk and edge elastic moduli of phosphorene (see table 4) and graphene (see table 5)

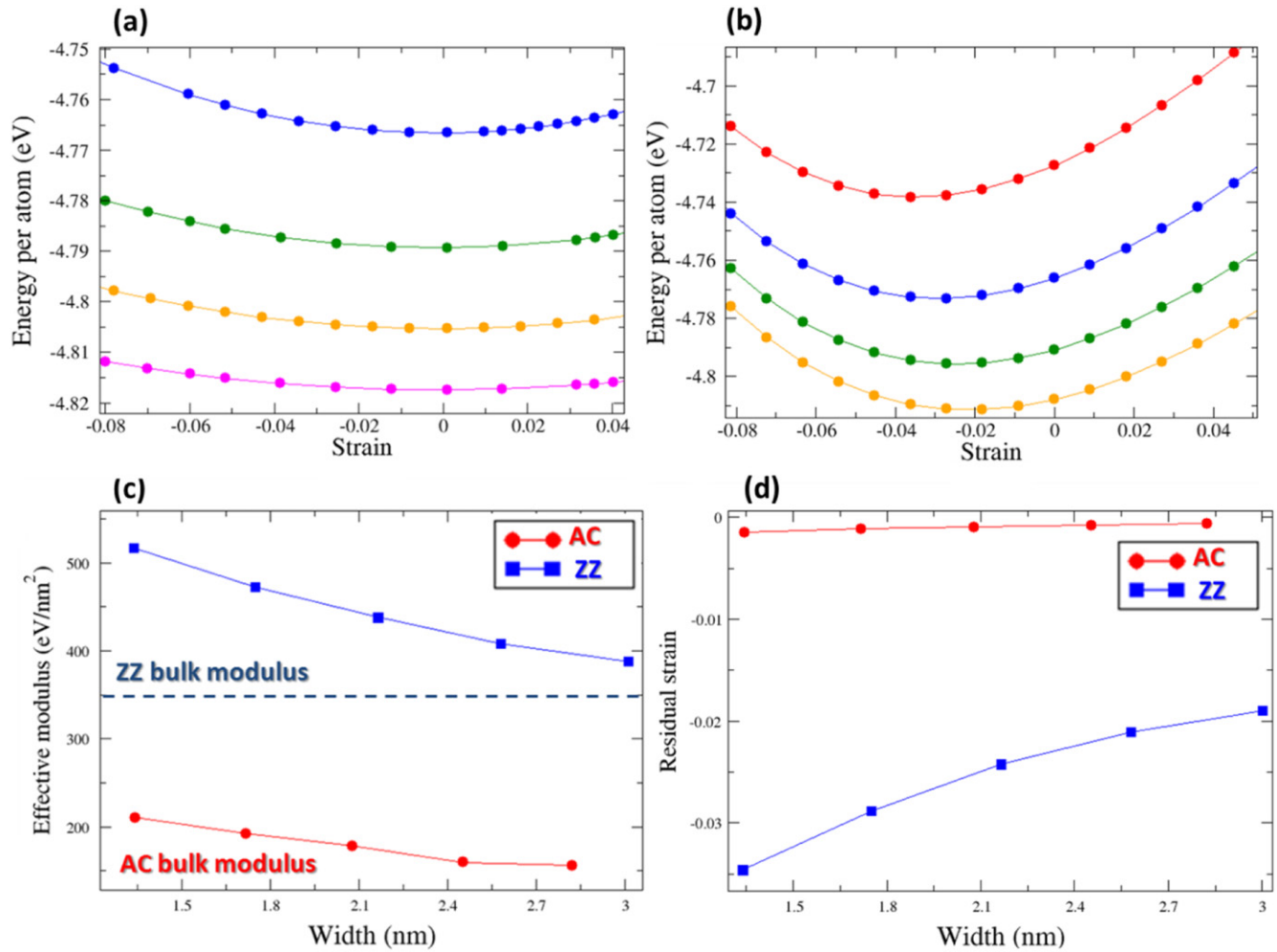


**Figure 8.** (a) Potential energy per atom as a function of applied strain for the AC PNRs with different ribbon widths: blue circles  $w = 16.37$  Å, green circles  $w = 19.9$  Å, yellow circles  $w = 23.4$  Å and magenta circles  $w = 26.29$  Å. (b) Potential energy per atom as a function of applied strain for the ZZ PNRs with different ribbon widths: red circles  $w = 13.22$  Å, blue circles  $w = 17.32$  Å, green circles  $w = 22.06$  Å and yellow circles  $w = 26.3$  Å. (c) Effective elastic modulus versus ribbon width for both AC (red circles) and ZZ (blue squares) PNRs. The bulk moduli along the ZZ and AC directions are indicated by the dashed lines. (d) Residual strain versus ribbon width for both AC (red circles) and ZZ (blue squares) PNRs.

**Table 4.** Calculated values of the bulk and edge elastic moduli, as well as the edge stresses for the AC and ZZ phosphorene nanoribbons.

Edge structure	Young's modulus, $E_b$ (eV nm <sup>-2</sup> )	Edge elastic constant, $E_e$ (eV nm <sup>-1</sup> )	Edge stress, $\tau$ (eV nm <sup>-1</sup> )
AC	138.1	42.1	2.13
ZZ	327.7	148.8	6.5

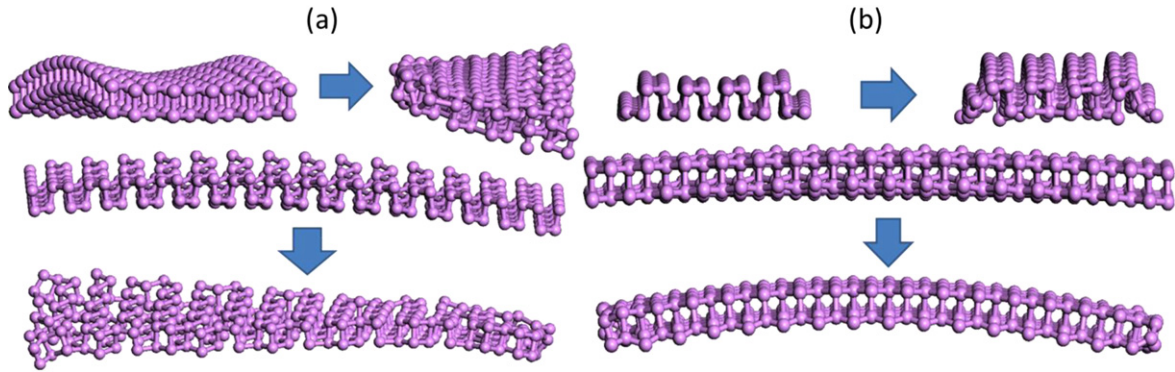
nanoribbons. As can be seen in these tables, the GNR bulk and edge elastic moduli, as well as the edge stresses are significantly larger than those of PNRs. This difference is due to their electronic structure. The puckered structure of phosphorene is a result of  $sp^3$  bonding between phosphorous atoms. This puckered structure maximizes the distance between the lone electron pairs situated at each atom (the lone pairs are located above and below the phosphorene plane in an alternating fashion). The high strength of graphene and the accordingly large elastic moduli can be attributed to its tight  $sp^2$  bonding between carbon atoms.

### 3.3. Edge stress-induced PNR distortions

It is well-known that the edge stress can lead to the warping, twisting and curling of GNRs [60, 62, 63, 65]. These structure distortions arise from the competition between the energy gain due to the reduction of the in-plane deformation energy, and the energy loss due to the out-of-plane bending energy of GNRs [60, 62, 63, 65]. Guided by the similarity of the edge properties between GNRs and PNRs, we examined the distortion of PNRs. To investigate the instability of flat PNRs, their initial planar shape was perturbed by applying the out-of-plane perturbation with the form of  $\zeta = A \exp(-y/\eta) \sin(\pi x/L)$ , where  $A$  is the amplitude of the

**Table 5.** Calculated values of the bulk and edge elastic moduli, as well as the edge stresses for the AC and ZZ graphene nanoribbons. Taken from [60].

Edge structure	Young's modulus, $E_b$ (eV nm <sup>-2</sup> )	Edge elastic constant, $E_e$ (eV nm <sup>-1</sup> )	Edge stress, $\tau$ (eV nm <sup>-1</sup> )
AC	1874.1	147.16	-20.58
ZZ	1878.5	112.63	-10.5

**Figure 9.** Distortion of PNRs induced by edge stress: (a) AC PNR and (b) ZZ PNR. From left to right: the initial and final configurations (front view). From top to bottom: the initial and final configurations (side view). For both the AC and ZZ PNRs, the length is  $\sim 60$  Å and the width is  $\sim 10$  Å.

edge perturbation,  $\eta$  is the length scale over which this perturbation penetrates into the nanoribbon, and  $L$  is the length of the nanoribbon along the  $X$ -direction. After the initial perturbation, the geometry of the PNR was optimized by minimizing the potential energy. The initial and final configurations are shown in figure 9. It is seen that although the size of our PNRs is limited in comparison to GNRs studied in [60, 62, 63, 65], the results of energy minimization clearly show the distortion of the PNRs due to the edge stress. More specifically, the ZZ PNR is arched, while the AC PNR is both curled and twisted after the energy minimization. The magnitude of the arching deformation (the maximal out-of-plane deviation from the reference flat geometry) for the AC PNR (see figure 9(a)) is  $\delta \approx 1.5$  Å and that for the ZZ PNR (see figure 9(b)) is  $\delta \approx 2.5$  Å. Clearly the amplitude of distortion in the AC PNR is smaller than that in the ZZ PNR since the edge stress of the former is smaller than that of the latter. The energy difference between the initial and final configurations for the AC PNR (see figure 9(a)) is  $\Delta E = 0.028$  eV, and that of the ZZ PNR is  $\Delta E = 0.049$  eV (see figure 9(b)).

We found that, as in the case of GNRs, the final shape of PNRs can be, to some extent, dependent on the initial perturbations [60, 62, 63, 65]. By using different types of perturbations, including random displacement perturbations in the out-of-plane direction, we found that the ZZ PNR is mostly arched, while the AC PNR is mostly both curled and twisted after the energy minimization. However, the final shapes (which are notably different from each other) are nearly degenerate in energy. Since the energy difference between the initial flat and the final deformed configuration is

comparable to  $k_b T$  (at room temperature,  $k_b T \approx 0.026$  eV), it is expected thermal fluctuations at room temperature can cause frequent switching between these nearly energy degenerate configurations.

#### 4. Conclusions

Using DFTB calculations, we examined the edge structures and elastic properties of both AC and ZZ PNRs. The edge relaxation, manifesting itself in the adjustment of the bond length and bond angles of the edge atoms, was examined in details. We found that the edge relaxation leads to the noticeable contraction of the vertically-oriented bonds of the edge atoms in AC PNRs, and horizontally-oriented bonds in ZZ PNRs. The effective width of the edge region, which includes all the atoms involved in the edge relaxation, was found to contain approximately three atomic rows near the edge for both AC and ZZ PNRs. In addition to these structural changes, the edge relaxation also leads to tensile stress at the PNR edges and also compressive residual strain in the PNR interior. We also calculated the magnitude of the edge stress and elastic edge modulus. It was found that these edge properties are sensitive to the edge types and show a strong anisotropy: the edge elastic constant and edge stress of ZZ PNRs are roughly three times larger than those of AC PNRs. Our calculations also show that the tensile edge stress can lead to the elastic distortion of PNRs. The present work may provide useful insights and guidelines for the fabrication and design of PNRs.

## Acknowledgments

The authors are grateful for the financial support from A\*Star, Singapore and the use of supercomputing facilities at ACRC, Singapore.

## References

- [1] Brent J R, Savjani N, Lewis E A, Haigh S J, Lewis D J and O'Brien P 2014 *Chem. Commun.* **50** 13338
- [2] Xia F, Wang H and Jia Y 2014 *Nat. Commun.* **5** 4458
- [3] Castellanos-Gomez A *et al* 2014 *2D Mater.* **1** 025001
- [4] Ling X, Wang H, Huang S, Xia F and Dresselhaus M S 2015 *Proc. Natl Acad. Sci.* **112** 201416581
- [5] Lu W, Nan H, Hong J, Chen Y, Zhu C, Liang Z, Ma X, Ni Z, Jin C and Zhang Z 2014 *Nano Res.* **7** 853
- [6] Novoselov K S, Geim A K, Morozov S V, Jiang D, Zhang Y, Dubonos S V, Grigorieva I V and Firsov A A 2004 *Science* **306** 666
- [7] Geim A 2009 *Science* **324** 1530
- [8] Watanabe K, Taniguchi T and Kanda H 2004 *Nat. Mater.* **3** 404
- [9] Song L *et al* 2010 *Nano Lett.* **10** 3209
- [10] Kim K K, Hsu A, Jia X, Kim S M, Shi Y, Dresselhaus M, Palacios T and Kong J 2012 *ACS Nano* **6** 8583
- [11] Mak K F, Lee C, Hone J, Shan J and Heinz T F 2010 *Phys. Rev. Lett.* **105** 136805
- [12] Radisavljevic B, Radenovic A, Brivio J, Giacometti V and Kis A 2011 *Nat. Nanotechnology* **6** 147
- [13] Sorkin V, Pan H, Shi H, Quek S Y and Zhang Y W 2014 *Crit. Rev. Solid State Mater. Sci.* **39** 319
- [14] Chhowalla M, Shin H S, Eda G, Li L-J, Loh K P and Zhang H 2013 *Nat. Chem.* **5** 263
- [15] Du Y, Liu H, Deng Y and Ye P D 2014 *ACS Nano* **8** 10035
- [16] Liu H, Neal A T, Si M, Du Y and Ye P D 2014 *IEEE Electron Device Lett.* **35** 795
- [17] Li L, Yu Y, Ye G J, Ge Q, Ou X, Wu H, Feng D, Chen X H and Zhang Y 2014 *Nat. Nanotechnology* **9** 372
- [18] Wu Q, Shen L, Yang M, Huang Z and Feng Y P 2014 arXiv:1405.3077
- [19] Reich E S 2014 *Nature* **506** 19
- [20] Low T, Engel M, Steiner M and Avouris P 2014 *Phys. Rev. B* **90** 081408
- [21] Koenig S P, Doganov R A, Schmidt H, Castro Neto A H and Özyilmaz B 2014 *Appl. Phys. Lett.* **104** 103106
- [22] Kou L, Frauenheim T and Chen C 2014 *J. Phys. Chem. Lett.* **5** 2675
- [23] Fei R, Faghaninia A, Soklaski R, Yan J-A, Lo C and Yang L 2014 *Nano Lett.* **14** 6393
- [24] Ong Z-Y, Cai Y, Zhang G and Zhang Y-W 2014 *J. Phys. Chem. C* **118** 25272
- [25] Zhang J, Liu H J, Cheng L, Wei J, Liang J H, Fan D D, Shi J, Tang X F and Zhang Q J 2014 *Sci. Rep.* **4** 6452
- [26] Zhao S, Kang W and Xue J 2014 *J. Mater. Chem. A* **2** 19046
- [27] Li W, Yang Y, Zhang G and Zhang Y-W 2015 *Nano Lett.* **15** 1961
- [28] Das S, Zhang W, Demarteau M, Hoffmann A, Dubey M and Roelofs A 2014 *Nano Lett.* **14** 5733
- [29] Cai Y, Zhang G and Zhang Y-W 2014 *Sci. Rep.* **4** 6677
- [30] Deng Y, Luo Z, Conrad N J, Liu H, Gong Y, Najmaei S, Ajayan P M, Lou J, Xu X and Ye P D 2014 *ACS Nano* **8** 8292
- [31] Buscema M, Groenendijk D J, Steele G A, van der Zant H S J and Castellanos-Gomez A 2014 *Nat. Commun.* **5** 4651
- [32] Sa B, Li Y-L, Qi J, Ahuja R and Sun Z 2014 *J. Phys. Chem. C* **118** 26560
- [33] Han X, Morgan Stewart H, Shevlin S A, Catlow C R A and Guo Z X 2014 *Nano Lett.* **14** 4607
- [34] Dai J and Zeng X C 2014 *J. Phys. Chem. Lett.* **5** 1289
- [35] Liu H, Neal A T, Zhu Z, Luo Z, Xu X, Tománek D and Ye P D 2014 *ACS Nano* **8** 4033
- [36] Qiao J, Kong X, Hu Z-X, Yang F and Ji W 2014 *Nat. Commun.* **5** 4475
- [37] Peng X, Wei Q and Copple A 2014 *Phys. Rev. B* **90** 1
- [38] Fei R and Yang L 2014 *Nano Lett.* **14** 2884
- [39] Rodin A S, Carvalho A and Neto A. H. Castro 2014 *Phys. Rev. Lett.* **112** 176801
- [40] Wei Q and Peng X 2014 *Appl. Phys. Lett.* **104** 251915
- [41] Çakır D, Sahin H and Peeters F M 2014 *Phys. Rev. B* **90** 205421
- [42] Elahi M, Khaliji K, Tabatabaei S M, Pourfath M and Asgari R 2014 *Phys. Rev. B* **91** 115412
- [43] Li Y, Yang S and Li J 2014 *J. Phys. Chem. C* **118** 23970
- [44] Taghizadeh Sisakht E, Zare M H and Fazileh F 2015 *Phys. Rev. B* **91** 085409
- [45] Jiang J-W and Park H S 2014 *J. Phys. D: Appl. Phys.* **47** 385304
- [46] Jiang J-W and Park H S 2014 *Nat. Commun.* **5** 4727
- [47] Hu T, Han Y and Dong J 2014 *Nanotechnology* **25** 455703
- [48] Qin G, Yan Q-B, Qin Z, Yue S-Y, Hu M and Su G 2015 *Phys. Chem. Chem. Phys.* **17** 4854
- [49] Glassbrenner C J and Slack G A 1964 *Phys. Rev.* **134** A1058
- [50] Yamasue E, Susa M, Fukuyama H and Nagata K 2002 *J. Cryst. Growth* **234** 121
- [51] Balandin A A 2011 *Nat. Mater.* **10** 569
- [52] Lv H Y, Lu W J, Shao D F and Sun Y P 2014 *Phys. Rev. B* **90** 085433
- [53] Carvalho A, Rodin A S and Neto A H C 2014 *EPL* **108** 47005
- [54] Guo H, Lu N, Dai J, Wu X and Zeng X C 2014 *J. Phys. Chem. C* **118** 14051
- [55] Maity A, Singh A and Sen P 2014 arXiv:1404.2469v2
- [56] Li W, Zhang G and Zhang Y-W 2014 *J. Phys. Chem. C* **118** 22368
- [57] Tran V and Yang L 2014 *Phys. Rev. B* **89** 235319
- [58] Peng X, Wei Q and Copple A 2014 *Phys. Rev. B* **90** 085402
- [59] Ramasubramaniam A and Muniz A R 2014 *Phys. Rev. B* **90** 085424
- [60] Shenoy V B, Reddy C D, Ramasubramaniam A and Zhang Y W 2008 *Phys. Rev. Lett.* **101** 245501
- [61] Jun S 2008 *Phys. Rev. B* **78** 073405
- [62] Reddy C D, Ramasubramaniam A, Shenoy V B and Zhang Y W 2009 *Appl. Phys. Lett.* **94** 101904
- [63] Bets K V and Yakobson B I 2009 *Nano Res.* **2** 161
- [64] Huang B, Liu M, Su N, Wu J, Duan W, Gu B L and Liu F 2009 *Phys. Rev. Lett.* **102** 166404
- [65] Shenoy V B, Reddy C D and Zhang Y W 2010 *ACS Nano* **4** 4840
- [66] Gan C K and Srolovitz D J 2010 *Phys. Rev. B* **81** 124445
- [67] Liu Y, Dobrinsky A and Yakobson B I 2010 *Phys. Rev. Lett.* **105** 235502
- [68] Branicio P S, Jhon M H, Gan C K and Srolovitz D J 2011 *Modelling Simul. Mater. Sci. Eng.* **19** 054002
- [69] Penev E S, Artyukhov V I, Ding F and Yakobson B I 2012 *Adv. Mater.* **24** 4956
- [70] Acik M and Chabal Y J 2011 *Japan. J. Appl. Phys.* **50** 070101
- [71] Koskinen P, Malola S and Häkkinen H 2008 *Phys. Rev. Lett.* **101** 115502
- [72] Klein D J and Bytautas L 1999 *J. Phys. Chem. A* **103** 5196
- [73] He K, Robertson A W, Lee S, Yoon E, Lee G and Warner J H 2014 *ACS Nano* **8** 12272
- [74] Yuan Q and Zhao Y P 2009 *J. Am. Chem. Soc.* **131** 6374
- [75] Won C Y, Joseph S and Aluru N R 2006 *J. Chem. Phys.* **125** 114701



- [76] Hou S, Shen Z, Zhao X and Xue Z 2003 *Chem. Phys. Lett.* **373** 308
- [77] Zheng W-T and Sun C Q 2011 *Energy Environ. Sci.* **4** 627
- [78] Slater J C and Koster G F 1954 *Phys. Rev.* **94** 1498
- [79] Langenberg D N and Peart R F 1964 *Science* **144** 1365
- [80] Ashcroft N and Mermin D 1976 *Solid State Physics* (New York: Thomson Learning) ch 22
- [81] Elstner M, Porezag D, Jungnickel G, Elsner J, Haugk M, Frauenheim T, Suhai S and Seifert G 1998 *Phys. Rev. B* **58** 7260
- [82] Frauenheim T, Seifert G, Elstner M, Hajnal Z, Jungnickel G, Porezag D, Suhai S and Scholz R 2000 *Phys. Status Solidi B* **217** 41
- [83] Wahiduzzaman M, Oliveira A F, Philipsen P, Zhechkov L, van Lenthe E, Witek H A and Heine T 2013 *J. Chem. Theory Comput.* **9** 4006
- [84] Kohn W and Sham L J 1965 *Phys. Rev.* **140** A1133
- [85] Burke K and Wagner L O 2013 *Int. J. Quantum Chem.* **113** 96
- [86] Burke K 2004 *The ABC of DFT* (Irvine, CA: University of California)
- [87] Seifert G and Hernández E 2000 *Chem. Phys. Lett.* **318** 355
- [88] Takao Y, Asahina H and Morita A 1981 *J. Phys. Soc. Japan* **50** 3362
- [89] Rudenko A N and Katsnelson M I 2014 *Phys. Rev. B* **89** 201408
- [90] Monkhorst H J and Pack J D 1976 *Phys. Rev. B* **13** 5188
- [91] Pack J D and Monkhorst H J 1977 *Phys. Rev. B* **16** 1748
- [92] Chadi D J and Cohen M L 1973 *Phys. Rev. B* **8** 5747
- [93] Goringe C M, Bowler D R and Hernández E 1999 *Rep. Prog. Phys.* **60** 1447
- [94] Luschtinetz R, Oliveira A F, Frenzel J, Joswig J-O, Seifert G and Duarte H A 2008 *Surf. Sci.* **602** 1347
- [95] Gaus M, Lu X, Elstner M and Cui Q 2014 *J. Chem. Theory Comput.* **10** 1518